Winter 12-18-2018

Numerical Simulations of Flow past a Triangular Airfoil and in a Sweeping Jet Actuator Using Different Turbulence Models

Han Yang
Washington University in St. Louis

WASHINGTON UNIVERSITY IN ST. LOUIS

School of Engineering and Applied Science

Department of Mechanical Engineering and Material Science

Thesis Examination Committee:

Ramesh Agarwal, Chair

Ling Zhou

Swami Karunamoorthy

Numerical Simulations of Flow past a Triangular Airfoil and in a Sweeping Jet Actuator Using Different Turbulence Models

by

Han Yang

A thesis presented to the School of Engineering and Applied Science of Washington University in partial fulfillment of the requirements for the degree of Master of Science

December 2018

St. Louis, Missouri

Dedicated to my parents

I want to dedicate my thesis to my dear parents (Mrs. Qiyun Yang and Mr. HuaGen Yang) and my beloved girlfriend (Qiong Wu) for their guidance, love and support.

Acknowledgements

First of all, I would like to thank my supervisor Professor Ramesh Agarwal. Since I joined the CFD lab, he has been treating me with great patience and kindness. He constantly gave me encouragement, which is of critical importance to me to stick to my research. I will never forget his guidance in my academic life.

Also, I would like to thank Dr. Ling Zhou. When I began to understand the project, I encountered lots of difficulties, such as how to use the CFD solver Fluent, how to generate a good mesh, etc. Dr. Ling Zhou gave me lot of advice and helped me in getting familiar with the project sooner than I could on my own. Also, Shuai Shuai provided me plenty of resources and references for my research and helped me with the mesh. Dr. Xu Han and Junhui Li gave me suggestions on improving the quality of my mesh and fixing the divergence in the solutions in many cases. I would like to sincerely thank all these people mentioned above as well as other students in the CFD lab.

I would also like to acknowledge my committee members, Dr. Ling Zhou and Dr. Karunarmoorthy for taking the time to read the thesis and attend its defense.

Han Yang

Washington University in St. Louis

December 2018

Contents

List of Figures

List of Tables

Abstract

Numerical Simulations of Flow past a Triangular Airfoil and in a Sweeping Jet Actuator Using Different Turbulence Models

by

Han Yang

Master of Science in Mechanical Engineering

Washington University in St. Louis

Research Adviser: Professor Ramesh Agarwal

The goal of this research is to perform 2D turbulent flow simulations to predict the flow past a triangular airfoil used for a Mars air vehicle and in a sweeping jet actuator used for active flow control. Simulations are performed using the commercial CFD software ANSYS Fluent.

The thesis consists of two parts. The first part of the thesis deals with the CFD simulations of a triangular airfoil in low-Reynolds-number compressible flow. This airfoil is one of the candidates for propeller blades on a possible future Martian air vehicle design. The aerodynamics and flow physics of the triangular airfoil is studied at angles of attack (AOA) from 0 deg. to 14 deg. at Mach number of 0.5. Compressible Reynold-Averaged Navier-Stokes (RANS) equations with a number of turbulence models, namely the SA, SST k-ω, and recently developed Wray – Agarwal (WA) model are solved. The computations are compared with the experimental data to assess the accuracy of various turbulence models. Lift coefficient, drag coefficient and pressure coefficient are obtained by performing computations at different angles of attack at a constant Mach number. It is shown that SST k-ω and WA model give the most accurate result.

The second part deals with the simulation of the unsteady oscillatory flow field of a Sweeping Jet Actuator (SWJ) used in active flow control of flow past wings. Based on recent experiments, sweeping jet actuators have been found to be more efficient for controlling flow separation in terms of mass flow requirements compared to constant blowing and suction or even synthetic jet actuators. They produce span-wise oscillating jets and therefore are called the sweeping jets. The frequency and span-wise sweeping extent depend on the geometric parameters and mass flow rate entering the actuators through the inlet section. The flow physics associated with these actuators is quite complex and is not fully understood at this time. The unsteady flow generated by such an actuator is simulated using the CFD solver ANSYS Fluent. k-ε model was used to get the computational results. Computed mean and standard deviation of velocity profiles generated by the actuator in quiescent air are compared with experimental data. Simulated results show good agreement with the experimentally observed trends with parametric variation of geometry and inflow conditions.

Chapter 1: Introduction

In this Chapter, the motivation behind this study and the background of the project are presented. It also introduces the outline of the thesis and a summary of the related published papers in the literature. The scope of the thesis is also included.

1.1 Motivation

The atmospheric conditions of Mars are different from the Earth. In these conditions, a specific type of wing and propeller for a Martian aircraft are required. To design an aircraft which could be used on Mars, a great deal of effort has been devoted in recent decades. The first step in this direction is to understand the airfoil performance of a Mars wing or propeller by using tools of Computational Fluid Dynamics (CFD). There has been rapid progress in the improvement of CFD tools namely the geometry modeling, grid generation, numerical algorithms and turbulence modeling for accurate and efficient solution of Reynolds-Averaged Navier-Stokes (RANS) equations for the flow field of airfoils like NACA0012, NACA4412, etc. However, few simulations and experiments have been conducted for a triangular airfoil which could be used on Mars. Horton has done research on laminar bubbles separation in low Reynolds number incompressible flow [1], the similar methodology can be used to study airfoil at low Reynolds number in compressible flow.

For reducing the noise and fuel burn of an aircraft, the active flow control (AFC) has been investigated in past several decades. Recently, sweeping jet actuator has been shown to be an effective AFC technology for improving the aerodynamic performance of high lift configurations

by reducing/mitigating the separated flow regions. Experiments on sweeping jet actuators have been conducted which are used in the thesis to validate the CFD simulations [2].

The motivation behind this study is to assess the relative accuracy of some widely used turbulence models by computing the flow fields of triangular airfoil and sweeping jet actuator.

1.2 Brief Review of Literature

Okamoto designed a Wind Tunnel to study the airfoil in the Martian atmosphere and conducted experiments on a triangular Mars airfoil. He found that the largest difference between the numerical simulations and experiments appeared at higher angles of attack [3]. Munday et al. employed a CFD code, CharLES, developed by Cascade Technologies, Inc. and the Center for Turbulence Research at Stanford University to study the flow field of a triangular airfoil [4]; three-dimensional low-Reynolds-number compressible flow simulations were performed using CharLES and the results were compared with the experiment.

For the sweeping jet actuator, Woszidlo and Wygnanski have discussed the geometric details and parameters governing the separation control from a sweeping jet actuator in the paper [2]. Vatsa et al. employed the commercial software PowerFLOW based on lattice Boltzmann method to study the flow field of a sweeping jet actuator using a number of turbulence models [5].

1.3 Scope of the Thesis

The Scope of the thesis is to conduct the computational study of the aerodynamics and flow fields of two configurations, the triangular airfoil and the sweeping jet actuator using various turbulence models and compare the CFD results with the experimental data and the

computational results from other papers, Spalart-Allmaras (SA) [6], SST *k-omega* [7], *k-epsilon* [8] and Wray-Agarwal (WA) [9] turbulence models are used in the numerical simulations.

Chapter 2: Methodology

In this section, the two configurations the triangular airfoil and the sweeping jet are introduced. The mesh generation and turbulence models are also introduced.

2.1 Geometries of Triangular Airfoil and Sweeping Jet Actuator

Flow field of two geometries are computed and analyzed in this thesis, namely the triangular airfoil and sweeping jet actuator as shown Figure 2.1 and Figure 2.2, respectively. The physical model of Martian airfoil used in the simulation is a triangular airfoil, it was used by Okamoto in his experimental study of the aerodynamic characterizations of the airfoil [3]. The chord length of the airfoil $c = 30\ mm$ and the maximum thickness is 1.5 mm. The triangular airfoil has 5% maximum thickness at 30% chord location as shown in Figure 2.1. The angles of attack (AOAs) vary from 0 deg. to 12 deg.

The sweeping jet actuator considered in this thesis has the internal chamber consisting of smooth curved edges instead of traditional actuator which has sharp corners. Woszidlo and Wygnanski provided the geometric details this actuator in their paper [2].

Figure 2. 1 Triangular Airfoil configuration

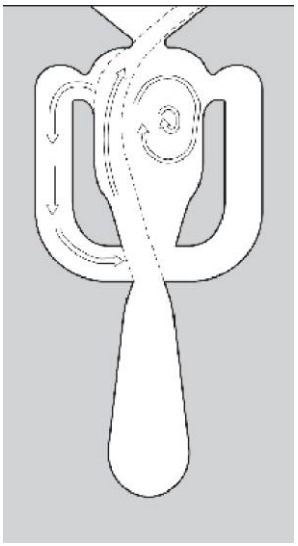

Figure 2. 2 Sweeping Jet Actuator configuration

2.2 Mesh Generation

ICEM CFD in ANSYS is used for geometry modeling and mesh generation. In the present study, two-dimensional numerical simulations are performed. A structured mesh is used for both the configurations, since the structured mesh requires less memory and provides better accuracy near the solid wall.

2.2.1 Triangular Airfoil Mesh

A rectangular computational domain is used as shown in Figure 2.3. The mid-chord location on the airfoil is the origin of the computational domain. The inlet, the top and the bottom boundaries are located 10c away from the mid-chord location of airfoil (origin) while the outlet is 20c away from the origin. The structured grid in the computational domain is generated using ICEM with grid clustering in regions of high velocity gradients. In region close to the airfoil surface, it is

ensured that y+ is < 1. For application of various turbulence models, there are enough layers of meshes inside the viscous sublayer to obtain good resolution of the turbulent boundary layer. Pressure far-field boundary conditions are employed at the inlet, bottom, top and outlet boundaries of the computational domain. At the airfoil, a no-slip wall boundary condition is used.

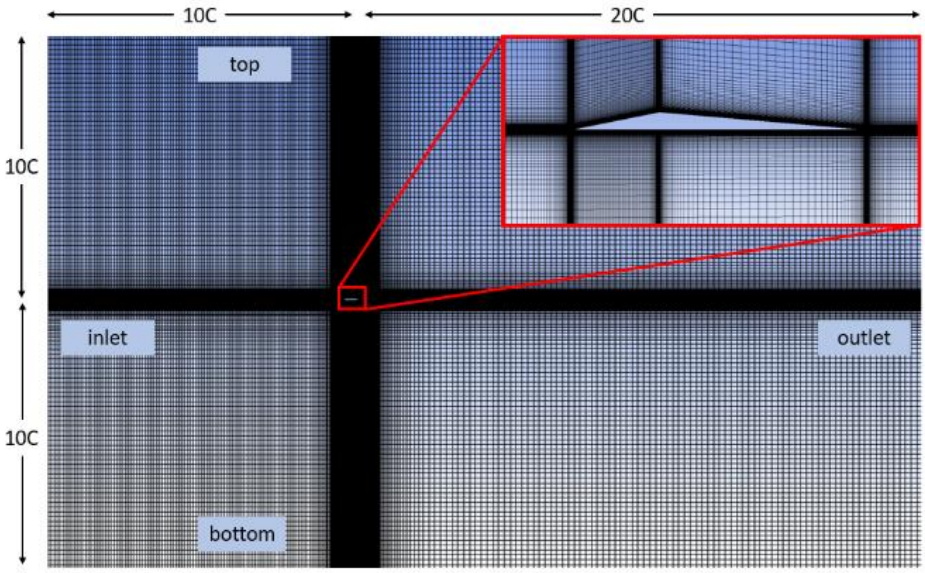

Figure 2. 3 Computational domain structured and mesh layout of triangular airfoil in unbounded flow

2.2.2 Sweeping Jet Actuator Mesh

Figure 2.4 shows the geometric model of sweeping jet actuator configuration. The model is so complex that it was separated it into 24 parts. For the nozzle part, blocks are separated into smaller parts to get more accurate description. Vatsa used the same model in his simulation and the grid in his simulation consisted of a total of 29.7 million cells [5].

Figure 2.5 (a) shows the computational domain and structured mesh for the sweeping jet actuator. The total number of nodes in this mesh is around 3.4 million. The outer part of the computational domain is shown below the actuator in Figure 2.5 (a). The outer part of the domain is large enough to ensure the boundary conditions would not affect the actuator flow. Figure 2.5 (b) - (d) show the details of the mesh inside the sweeping jet actuator. The mesh in the feedback channels and the nozzle is refined to ensure that simulation lead to accurate results. Computations show that the highest speed always occurs in the nozzle area, therefore the nozzle has relative finer grid compared to meshes in other parts of the actuator.

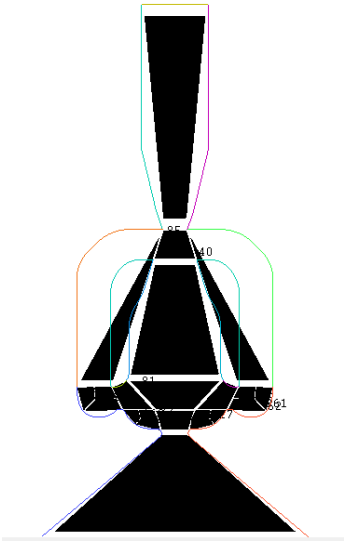

Figure 2. 4 Sweeping Jet Actuator

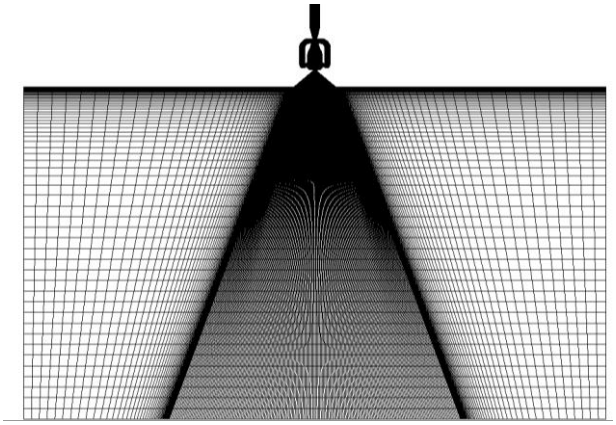

(a) Computational domain and structured mesh

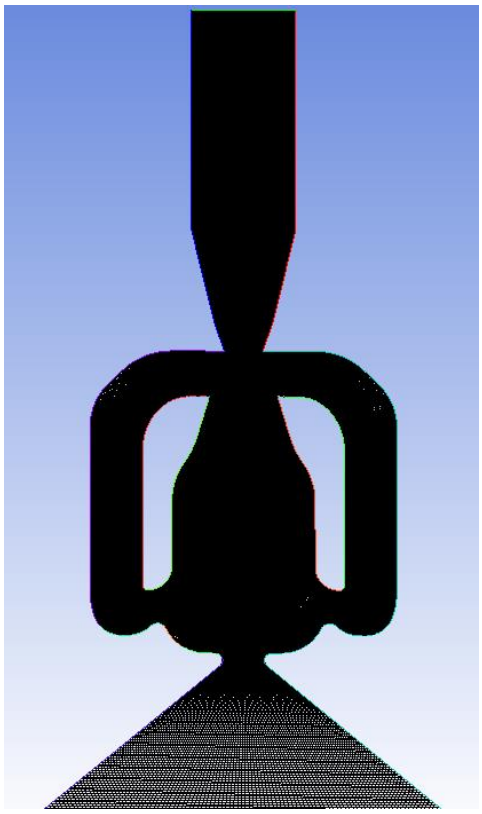

(b) Mesh inside the sweeping jet actuator

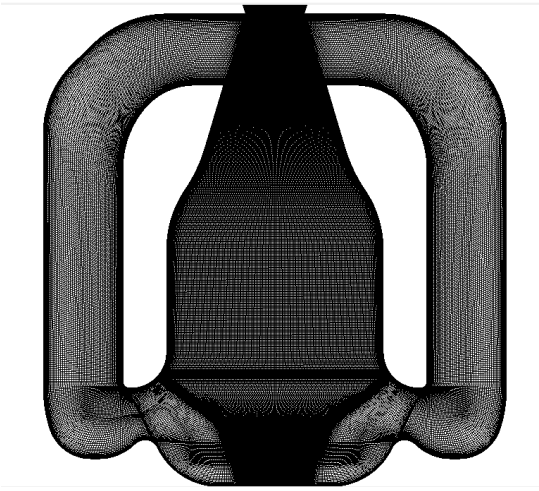

(c) Details of mesh in the middle part of sweeping jet actuator

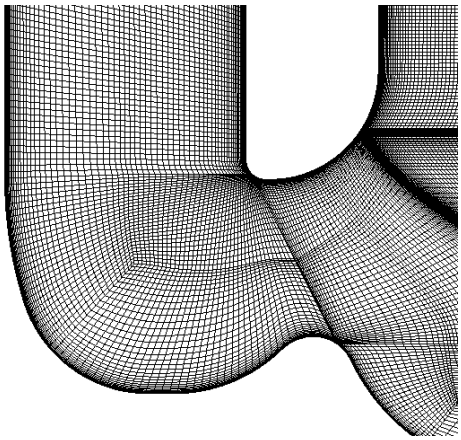

(d) Details of mesh in the feedback channel

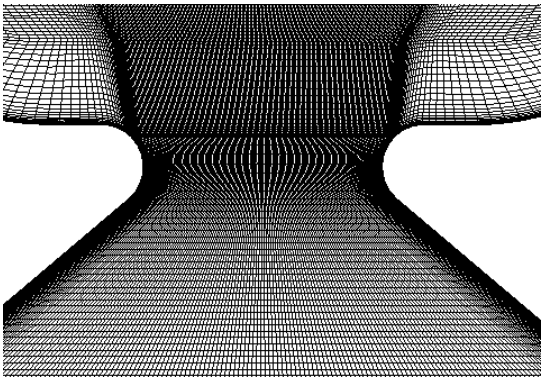

(e) Details of mesh in the nozzle

Figure 2. 5 2D structured mesh in various parts of the sweeping jet actuator

2.3 Validation of the Solution Methodology

2.3.1 Triangular Airfoil

For triangular airfoil, the double precision solver in ANSYS FLUENT 17.1 is used to perform the CFD simulations. Compressible Reynolds-averaged Navier - Stokes equations with a number of turbulence models, namely the SA [6], SST k-ω [7] and WA [9] models are solved. The pressure-coupled transient solver in FLUENT is used for pressure-velocity coupling. When $0° \leq \alpha < 8°$, the flow around the triangular airfoil remains essentially steady [10]. When $\alpha \geq 8°$,instability appears in the flow. Therefore, steady solver is employed for $0° \leq \alpha < 8°$. For $\alpha \geq 8°$, transient solver is employed.

A grid-refinement study was performed to ensure the grid independence of the solution. The study was performed based on the SST k-ω model for triangular airfoil at Re = 3000, M = 0.5 and α = 8 deg. The y+ of all meshes was less than 0.1 for the first mesh point away from the wall [4]. The results comparing solutions for different grid resolutions are summarized in Table 1. According to these results, medium-resolution grid is sufficient to obtain accuracy compared to the fine-resolution grid. Therefore, the medium grid is used in all simulations reported in this thesis.

Table 1 Grid-refinement study for flow past a triangular airfoil in unbounded flow based on SST k-ω turbulence model at Re = 3000, M = 0.5 & α = 8 deg.

Mesh	Cell numbers	y+	C_L	C_D
Experiment			0.54421	0.10169
DNS simulation			0.70167	0.12117
Coarse grid	86233	< 0.1	0.51032	0.08841
Medium grid	137676	< 0.1	0.52153	0.08933
Fine grid	420314	< 0.1	0.52831	0.08957

2.3.2 Sweeping Jet Actuator

This Computations are performed using the CFD software Fluent 17.1. Steady compressible Reynolds-Averaged Navier-Stokes (RANS) equations are solved using the finite volume method. *k-epsilon* two-equation model is used in this study. A second order upwind scheme is used for the convection terms and a second order central difference scheme is used for the diffusion terms. Coupled algorithm is employed for pressure-velocity coupling. A velocity inlet was applied to the inlet of the sweeping jet actuator and a constant pressure boundary condition was assigned at the outlet of the sweeping jet actuator [5]. A no-slip boundary condition was used on all the solid walls. The Computed solution is uploaded in CFD post for analysis of the numerical data.

2.4 Turbulence Models

The Spalart-Allmaras (SA) model [6] is currently the most widely used turbulence model in industry. The SA model is a one-equation model that solves a transport equation for the kinematic turbulent eddy viscosity. In its original form, the model is effectively a low-Reynolds number model requiring the viscosity-affected region of the boundary layer to be properly resolved. It takes a shorter time to converge compared to the SST *k-ω* model [7] and in competitive with the WA model [9].

2.4.1 Spalart-Allmaras (SA) Model

The standard SA model is governed by the following equation:

$$\frac{\partial \hat{v}}{\partial t} + u_j \frac{\partial \hat{v}}{\partial x_j} = c_{b1}(1 - f_{t2})\hat{S}\hat{v} - [c_{w1} f_w - \frac{c_{b1}}{\kappa^2} f_{t2}](\frac{\hat{v}}{d})^2 + \frac{1}{\sigma}[\frac{\partial}{\partial x_j}((v + \hat{v})\frac{\partial \hat{v}}{\partial x_j}) + c_{b2}\frac{\partial \hat{v}}{\partial x_i}\frac{\partial \hat{v}}{\partial x_i}] \qquad (1\text{-}1)$$

The turbulent eddy viscosity is computed from:

$$\mu_t = \rho \hat{\nu} f_{v1}$$

where

$$f_{v1} = \frac{X^3}{X^3 + c_{v1}^3}$$

$$X = \frac{\hat{\nu}}{\nu}$$

In above equation, ρ denotes density, μ denotes the molecular dynamic viscosity and $\nu = \mu / \rho$ denotes the molecular kinetic viscosity.

Other definitions of variables are:

$$\hat{S} = \Omega + \frac{\nu}{\kappa^2 d^2} f_{v2}$$

where $\Omega = \sqrt{2W_{ij}W_{ij}}$ is the magnitude of the vorticity.

$$f_{v2} = 1 - \frac{X}{1 + X f_{v1}} \qquad f_w = g\left[\frac{1 + c_{w3}^6}{g^6 + c_{w3}^6}\right]^{1/6}$$

$$g = r + c_{w2}(r^6 - r)$$

$$r = \min\left[\frac{\hat{\nu}}{\hat{S}\kappa^2 d^2}, 10\right]$$

$$f_{t2} = c_{t3} \exp(-c_{t4} X^2)$$

$$W_{ij} = \frac{1}{2}(\frac{\partial u_i}{\partial x_j} - \frac{\partial u_j}{\partial x_i})$$

Boundary conditions are:

$$\hat{v}_{wall} = 0$$

$$\hat{v}_{farfield} = 3v_{\infty} : to : 5v_{\infty}$$

The kinematic eddy viscosity values at wall and in the far field are:

$$v_{t,wall} = 0$$

$$v_{t,farfield} = 0.210438v_{\infty} : to : 1.294234v_{\infty}$$

The model constants are:

$$c_{b1} = 0.1355 \qquad \sigma = 2/3 \qquad c_{b2} = 0.622 \qquad \kappa = 0.41$$

$$c_{w2} = 0.3 \qquad c_{w3} = 2 \qquad c_{v1} = 7.1 \qquad c_{t3} = 1.2 \qquad c_{t4} = 0.5$$

$$c_{w1} = \frac{c_{b1}}{\kappa^2} + \frac{1 + c_{b2}}{\sigma}$$

2.4.2 *k*-ε Model

The standard *k*-ε model is one of the first two-equation *k*-ε model published in the turbulence modeling literature and has been extensively applied and modified for computing wide range of industrial flows. This model is included in FLUENT as a standard *k*-ε model and employs the wall function for computational efficiency. The transport equation for turbulent kinetic energy *k*

is an exact equation while the transport equation for turbulent dissipation (ε) is formulated using physical reasoning. The following are the transport equations for k and ε developed by Launder and Spalding [8].

$$\frac{\partial \rho k}{\partial t} + \frac{\partial \rho u_i k}{\partial x_i} = -\rho \overline{u_i u_j} \frac{\partial u_i}{\partial x_i} + \frac{\partial}{\partial x_i}\left[\rho\left(v_l + \frac{c_\mu k^2}{\sigma_k \epsilon}\right)\frac{\partial k}{\partial x_i}\right] - \rho\varepsilon \tag{1-2}$$

$$\frac{\partial \rho \varepsilon}{\partial t} + \frac{\partial \rho \mu_i \varepsilon}{\partial x_i} = -C_{\varepsilon 1}\rho \overline{u_i u_j} \frac{\partial \mu_i \varepsilon}{\partial x_i k} + \frac{\partial}{\partial x_i}\left[\rho\left(v_l + \frac{c_\mu k^2}{\sigma_\varepsilon \epsilon}\right)\frac{\partial \varepsilon}{\partial x_i}\right] - C_{\varepsilon 2}\rho\frac{\varepsilon^2}{k} \tag{1-3}$$

$$\mu_t = \frac{\rho C_\mu k^2}{\varepsilon}$$

The model constants are:

$$C_\mu = 0.09 \quad \sigma_k = 1.00 \quad \sigma_\varepsilon = 1.30 \quad C_{1\varepsilon} = 1.44 \quad C_{2\varepsilon} = 1.92$$

2.4.3 SST k-ω Model

The SST k-ω model is also governed by two transport equations [7]. This model is more complex than one-equation SA model and requires more computational cost for simulation.

The governing equations are:

$$\frac{\partial(\rho k)}{\partial t} + \frac{\partial(\rho u_j k)}{\partial x_j} = P - \beta^* \rho \omega k + \frac{\partial}{\partial x_j}[(\mu + \sigma_k \mu_t)\frac{\partial k}{\partial x_j}] \tag{1-4}$$

$$\frac{\partial(\rho \omega)}{\partial t} + \frac{\partial(\rho u_j \omega)}{\partial x_j} = \frac{\gamma}{v_t} P - \beta \rho \omega^2 + \frac{\partial}{\partial x_j}[(\mu + \sigma_\omega \mu_t)\frac{\partial \omega}{\partial x_j}] + 2(1 - F_1)\frac{\rho \sigma_{\omega 2}}{\omega}\frac{\partial k}{\partial x_j}\frac{\partial \omega}{\partial x_j} \tag{1-5}$$

P is defined as:

$$P = \tau_{ij} \frac{\partial u_i}{\partial x_j}$$

$$\tau_{ij} = \mu_t (2S_{ij} - \frac{2}{3} \frac{\partial u_k}{\partial x_k} \delta_{ij}) - \frac{2}{3} \rho k \delta_{ij}$$

$$S_{ij} = \frac{1}{2} (\frac{\partial u_i}{\partial x_j} + \frac{\partial u_j}{\partial x_i})$$

The turbulent eddy viscosity is computed from:

$$\mu_t = \frac{\rho a_1 k}{\max(a_1 \omega, \Omega F_2)}$$

Inner and outer constant are combined as:

$$\phi = F_1 \phi_1 + (1 - F_1) \phi_2$$

where

$$F_1 = \tanh(\arg_1^4)$$

$$\arg_1 = \min[\max(\frac{\sqrt{k}}{\beta^* \omega d}, \frac{500\nu}{d^2 \omega}), \frac{4\rho \sigma_{\omega 2} k}{CD_{kw} d^2}]$$

$$CD_{kw} = \max(2\rho \sigma_{\omega 2} \frac{1}{\omega} \frac{\partial k}{\partial x_j} \frac{\partial \omega}{\partial x_j}, 10^{-20})$$

$$F_2 = \tanh(\arg_2^2)$$

$$\arg_2 = \max(2 \frac{\sqrt{k}}{\beta^* \omega d}, \frac{500\nu}{d^2 \omega})$$

$\Omega = \sqrt{2W_{ij}W_{ij}}$ is the magnitude of vorticity:

$$W_{ij} = \frac{1}{2}(\frac{\partial u_i}{\partial x_j} - \frac{\partial u_j}{\partial x_i})$$

Boundary conditions are:

$$\frac{U_\infty}{L} < \omega_{farfield} < 10\frac{U_\infty}{L}$$

$$\frac{10^{-5}U_\infty^2}{\mathrm{Re}_L} < k_{farfield} < \frac{0.1U_\infty^2}{\mathrm{Re}_L}$$

$$\omega_{wall} = 10\frac{6\nu}{\beta_1(\Delta d_1)^2}$$

$$k_{wall} = 0$$

The model constants are:

$$\gamma_1 = \frac{\beta_1}{\beta^*} - \frac{\sigma_{\omega 1}\kappa^2}{\sqrt{\beta^*}} \qquad \gamma_2 = \frac{\beta_2}{\beta^*} - \frac{\sigma_{\omega 2}\kappa^2}{\sqrt{\beta^*}}$$

$$\sigma_{k1} = 0.85 \qquad \sigma_{\omega 1} = 0.5 \qquad \beta_1 = 0.075$$

$$\sigma_{k2} = 1.0 \qquad \sigma_{\omega 2} = 0.856 \qquad \beta_2 = 0.0828$$

$$\beta^* = 0.09 \qquad \kappa = 0.41 \qquad a_1 = 0.31$$

2.4.4 Wray-Agarwal (WA 2017) Turbulence Model

The original one-equation WA2017 turbulence model [9] was derived from the SST *k-ω* model for the eddy viscosity $R = k/\omega$. The *R*-Equation of WA2017 model can be written as:

$$\frac{\partial R}{\partial t} + \frac{\partial u_j R}{\partial x_j} = \frac{\partial}{\partial x_j}\left[(\sigma_R R + \nu)\frac{\partial R}{\partial x_j}\right] + C_1 RS + f_1 C_{2k\omega}\frac{R}{S}\frac{\partial R}{\partial x_j}\frac{\partial S}{\partial x_j} - (1 - f_1)C_{2k\varepsilon}R^2\left(\frac{\frac{\partial S}{\partial x_j}\frac{\partial S}{\partial x_j}}{S^2}\right) \quad (1\text{-}6)$$

The turbulent eddy viscosity is given by the equation:

$$\nu_T = f_\mu R$$

The wall blocking effect is accounted for by the damping function f_μ. The value of C_w was determined by calibrating the model to a simple flat plate flow. ν has the usual definition of dynamic viscosity.

$$f_\mu = \frac{\chi^3}{\chi^3 + C_w^3}, \qquad \chi = \frac{R}{\nu}$$

S is the mean strain described below.

$$S = \sqrt{2S_{ij}S_{ij}}, \qquad S_{ij} = \frac{1}{2}\left(\frac{\partial u_i}{\partial x_j} + \frac{\partial u_j}{\partial x_i}\right)$$

The model can behave either as a one equation *k-ω* or one equation *k-ε* model based on the switching function f_1. The switching function f_1 is limited by an upper bound of 0.9 for better stability.

$$f_1 = min(tanh(arg_1^4), 0.9)$$

$$arg_1 = \frac{1 + \frac{d\sqrt{RS}}{\nu}}{1 + \left[\frac{max\left(d\sqrt{RS}, 1.5R\right)}{20\nu}\right]^2}$$

The values of constants used in WA2017 model are listed below.

$$C_{1k\omega} = 0.0829 \quad C_{1k\varepsilon} = 0.1127$$

$$C_1 = f_1(C_{1k\omega} - C_{1k\varepsilon}) + C_{1k\varepsilon}$$

$$\sigma_{k\omega} = 0.72 \quad \sigma_{k\varepsilon} = 1.0$$

$$\sigma_R = f_1(\sigma_{k\omega} - \sigma_{k\varepsilon}) + \sigma_{k\varepsilon}$$

$$\kappa = 0.41$$

$$C_{2k\omega} = \frac{C_{1k\omega}}{\kappa^2} + \sigma_{k\omega} \quad C_{2k\varepsilon} = \frac{C_{1k\varepsilon}}{\kappa^2} + \sigma_{k\varepsilon}$$

$$C_w = 8.54$$

Chapter 3: Analysis of Triangular Airfoil

In this Chapter, the computational analysis of the flow field of triangular airfoil is presented using different turbulence models. The computations are compared with experimental data and the computations of other investigations.

3.1 Lift Coefficient Analysis

The results for $Re = 3000$ and $M = 0.5$ are presented in Figures. 3.1-3.4. In these figures, 'DNS' labeled results are from Munday et al. obtained using the CFD code, CharLES [4], 'experiment' denotes the experiment results from a Mars Wind Tunnel test on a scaled model at the same Reynolds number and Mach number [3], and 'SA', 'SST' and 'WA' denote the present computational results obtained with SA model, SST *k*-ω and WA model, respectively. Figures 3.1-3.4 show the comparison of results based on different turbulence models with experimental data for the lift coefficient at various angles of attack α. In Figure 3.4, present SA result is very close to those of Munday et al. [3] when $0° \leq \alpha \leq 8°$. SST *k*-ω result shows better agreement when $8° \leq \alpha \leq 14°$ compare to the SA model. However, WA model results show the best agreement with the experimental data, especially when $8° \leq \alpha \leq 14°$. In Figure 3.4, DNS result shows large discrepancy when $8° \leq \alpha \leq 14°$. Although there exists small error between the experimental results and WA model results. WA model result is still the best which has the least error e_m compared to the SA and SST *k*-ω model. In Figure 3.4, the result of DNS in incompressible flow is also shown. This computation was performed by Zhang et al. [11] and is clearly worse than DNS in compressible flow.

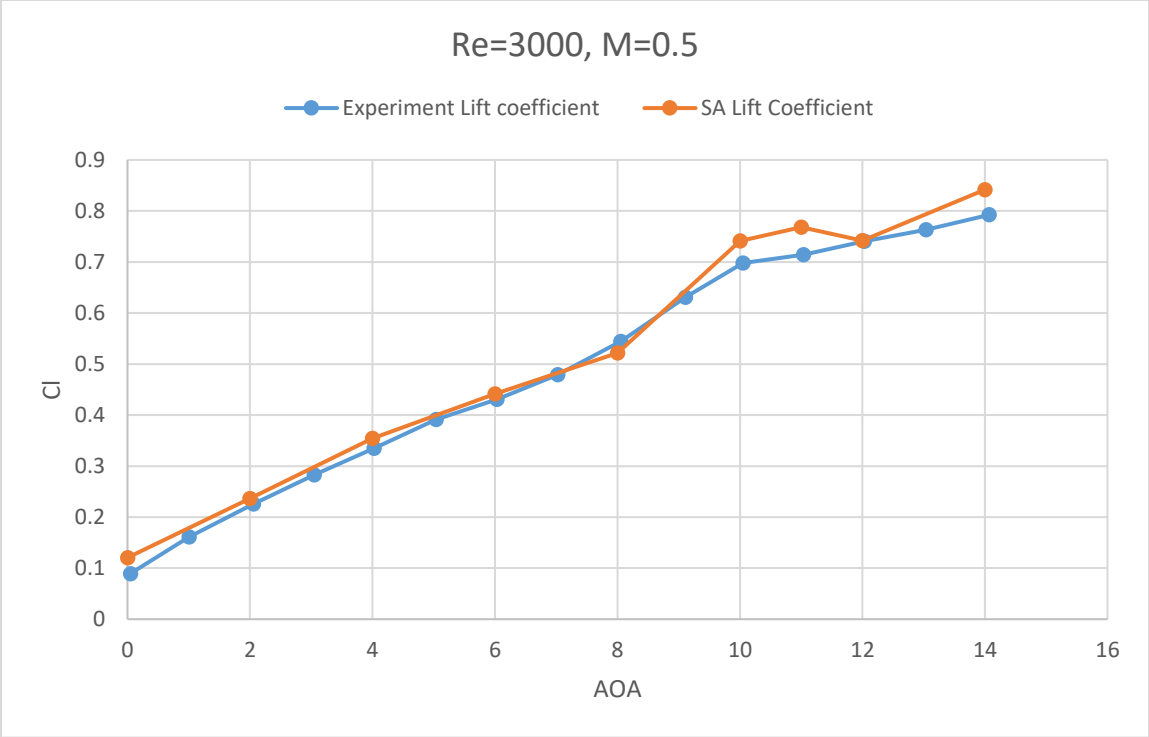

Figure 3. 1 Lift coefficient vs. AOA curve for Triangular Airfoil based on SA model

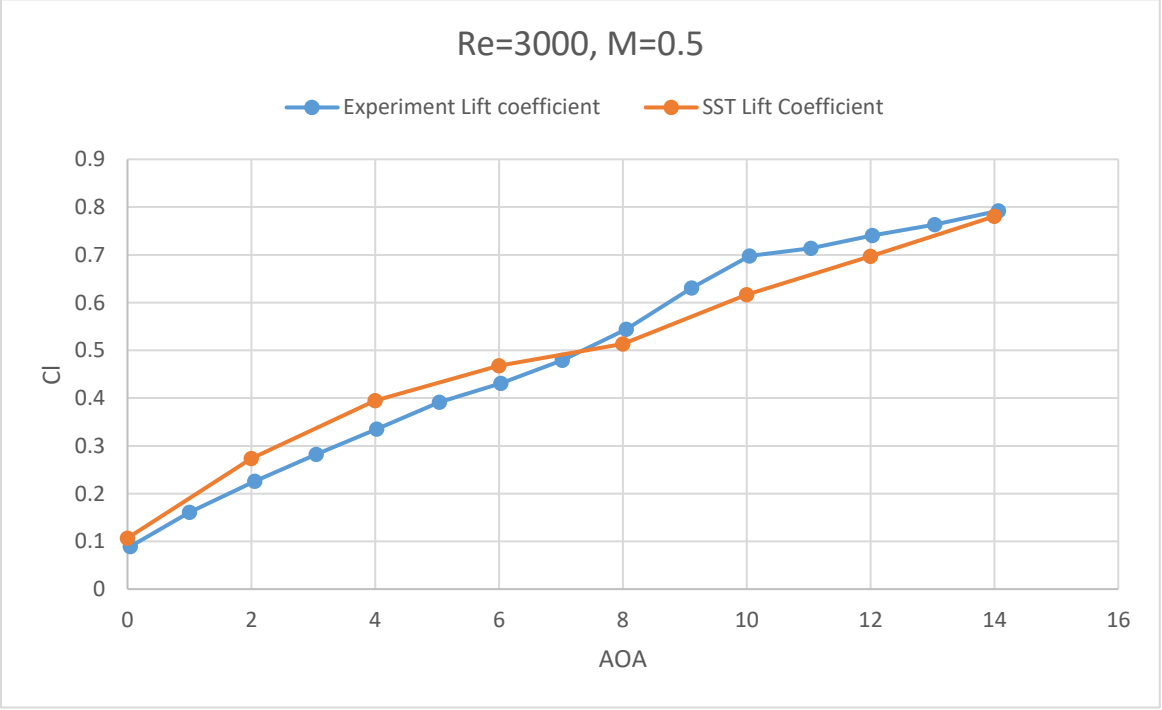

Figure 3. 2 Lift coefficient vs. AOA curve for Triangular Airfoil based on SST *k-ω* model

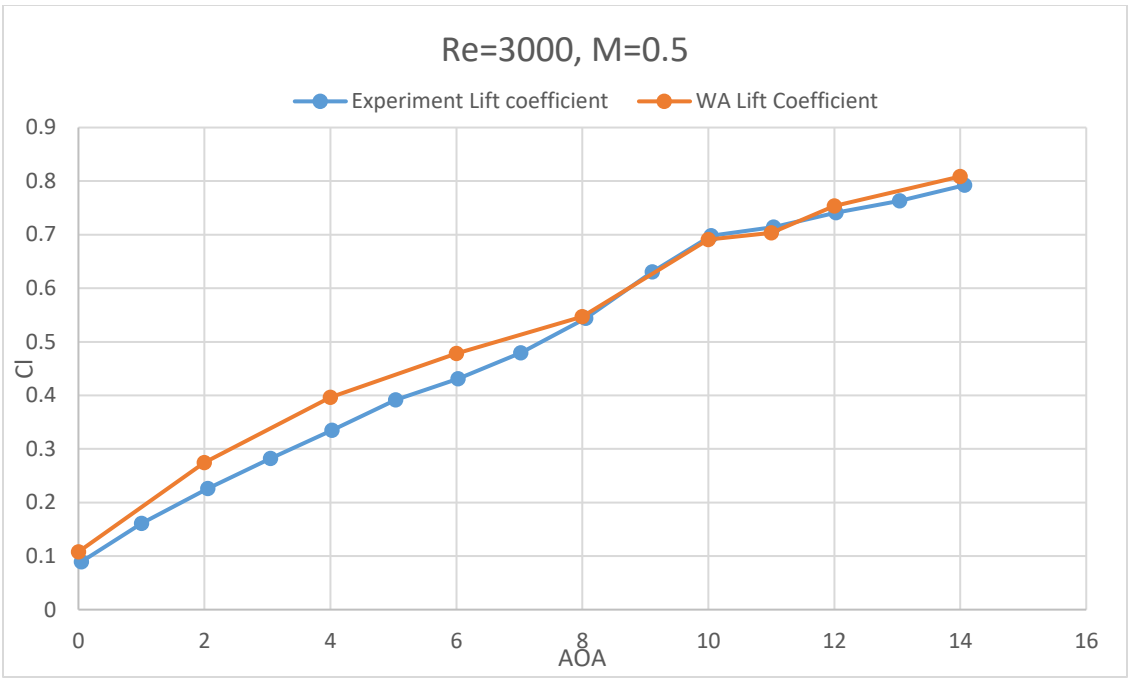

Figure 3. 3 Lift coefficient vs. AOA curve for Triangular Airfoil based on WA model

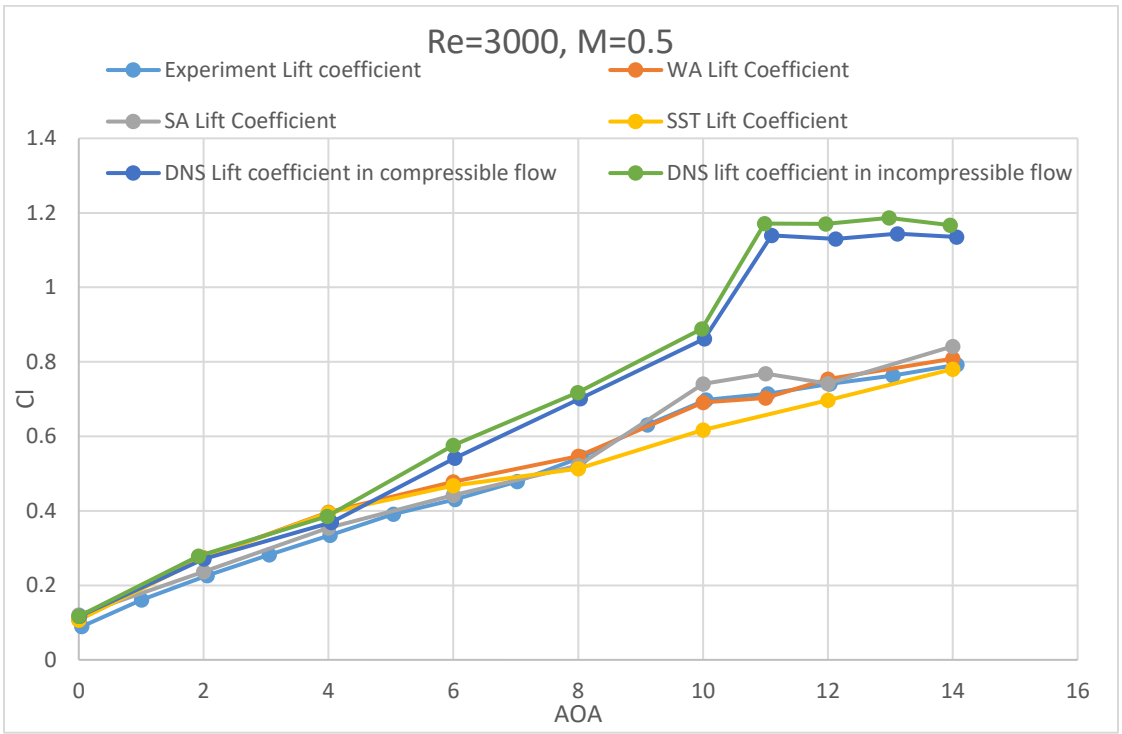

Figure 3. 4 Comparison of Lift Coefficient vs. AOA for Triangular Airfoil using SA, SST *k-ω* and WA turbulence model, and DNS (incompressible & compressible) and experimental data

3.2 Drag Coefficient Analysis

The results when $Re = 3000$, $M = 0.5$ are presented in Figures. 3.5-3.7. In wind tunnel experiment, errors can be generated because of vibration of the wing model, boundaries of the wind tunnel, and gas pulsation, etc. The C_d increases as the AOA increases. There still exist differences between the computational result and the experiment data although corrections have been added to the wind tunnel results [4]. Again, the WA model shows the best agreement with the experimental results. The greater is AOA, the more accurate is the WA model. These curves for drag coefficient are fairly close using the three turbulence models except for the first few points obtained from the computations using the WA model. In particular when AOA is from 0 deg. to 4 deg. As shown in Figure 3.7. Computational results from WA model, when AOA from 6 deg. to 14 deg. are in general give in good agreement with the experimental data. As shown in Figure 3.8, both SST k-ω and WA model give relatively good results. Figure 3.8 also shows the comparison of DNS for both incompressible and compressible flow. The DNS for incompressible flow was performed by Zhang et al. [11]. It is obvious that the DNS results in compressible flow have better agreement with experimental data compared to the DNS results in incompressible flow.

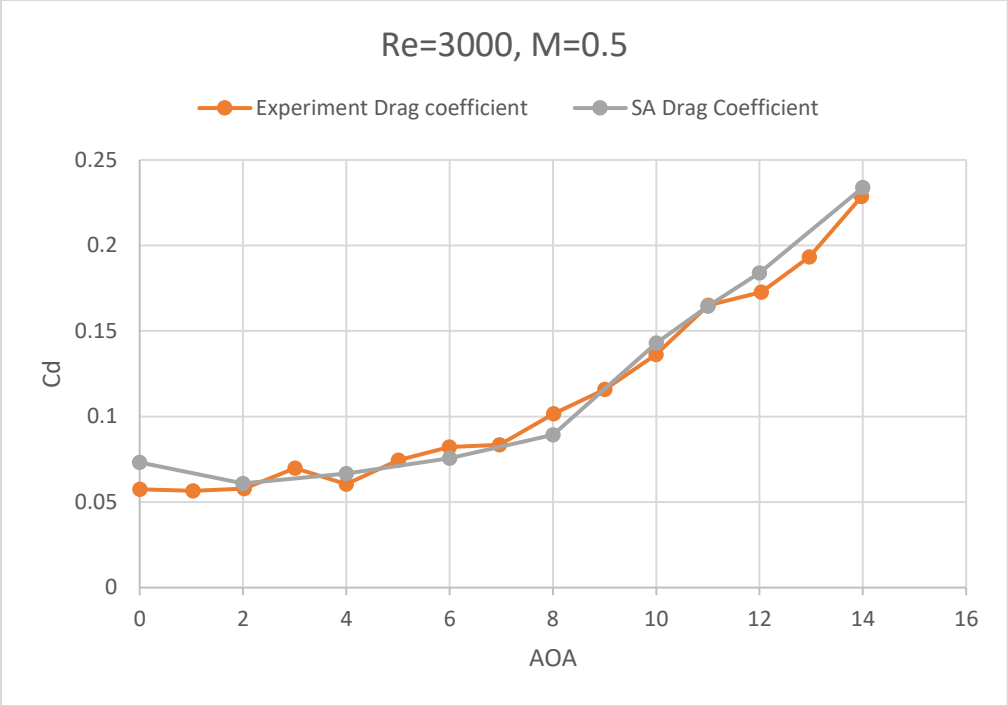

Figure 3. 5 Drag coefficient vs. AOA curve for Triangular Airfoil based on SA model

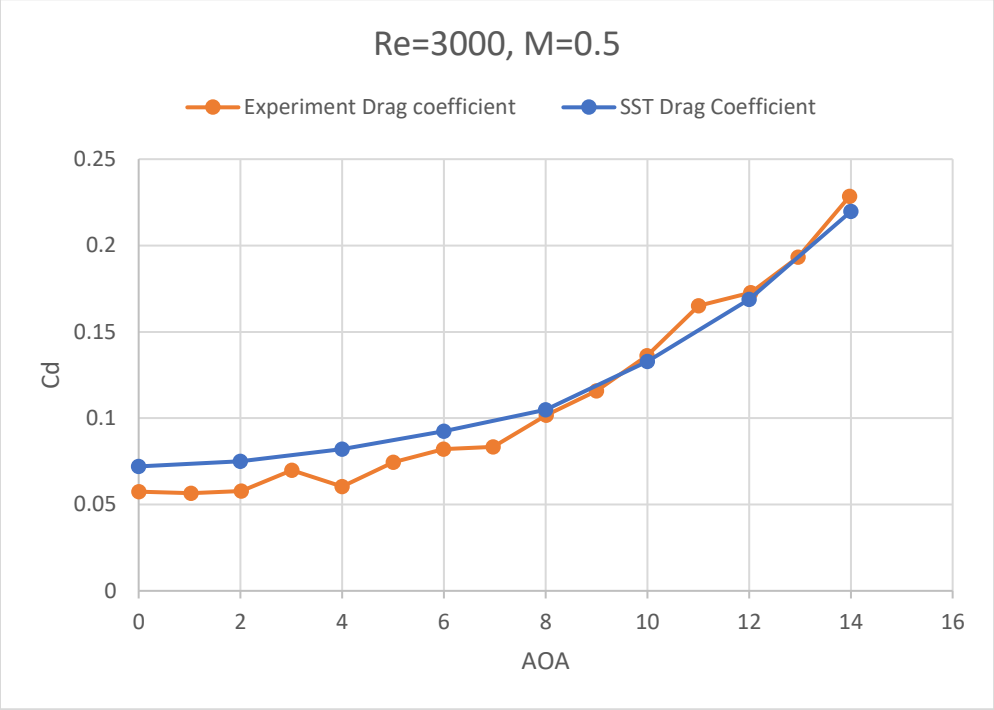

Figure 3. 6 Drag coefficient vs. AOA curve for Triangular Airfoil based on SST *k-ω* model

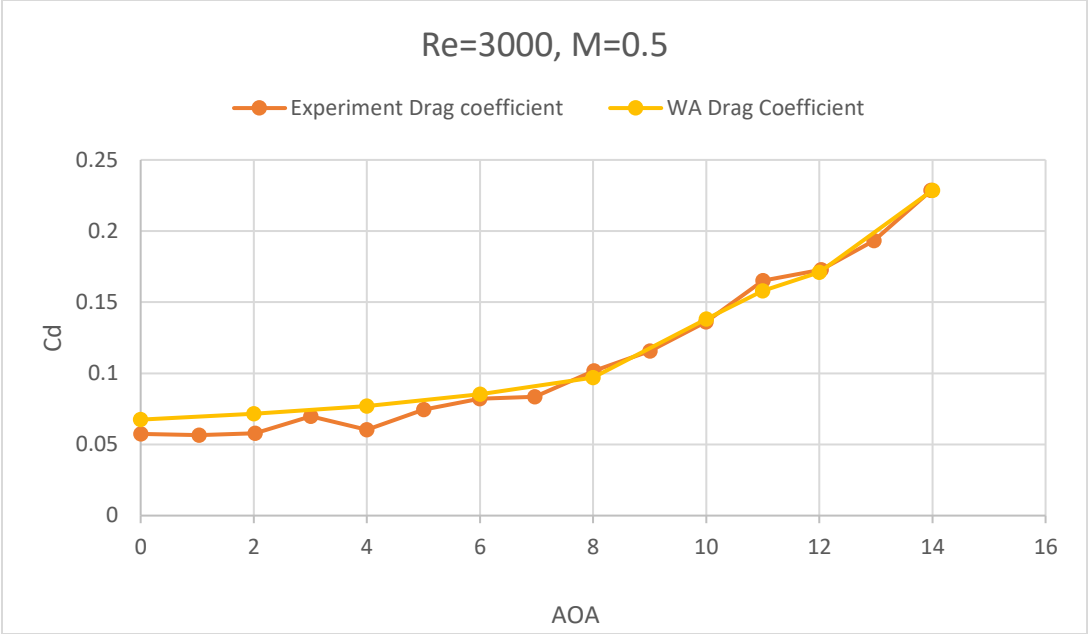

Figure 3. 7 Drag coefficient vs. AOA curve for Triangular Airfoil based on WA model

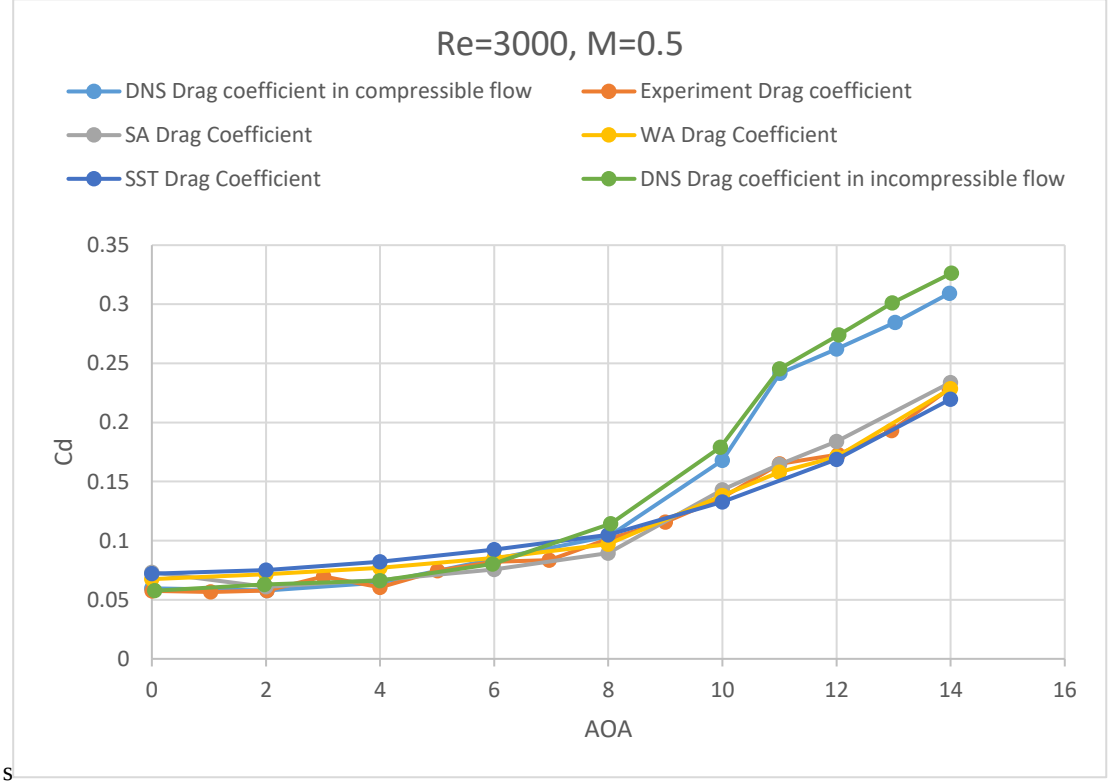

s

Figure 3. 8 Comparison of Drag Coefficient vs. AOA for Triangular Airfoil using SA, SST *k-ω* and WA turbulence model, and DNS (incompressible & compressible) and experimental data

3.3 Pressure Distribution on Triangular Airfoil

Figures 3.9 and 3.10 show the pressure coefficient on the top surface of the triangular airfoil. Three computational results are compared with the experimental data and DNS data from Munday et al. research [4]. The comparisons are shown for the case of *Re* = 3000 and *M* = 0.5 when α = 6 deg. and 12 deg. For these two AOAs, good agreement is obtained. The C_P on the leading edge is lower than that on the trailing edge on the upper surface of the airfoil. C_P on the lower surface of the airfoil is larger than that on the upper surface of the airfoil as expected. The maximum of C_P appears at the trailing edge of the airfoil. Figure 3.11 shows the pressure contours on triangular airfoil at various angles of attack. At angle of attack greater than 8 deg., vortex shedding from the trailing edge of the airfoil can be seen.

The C_P on the leading edge is lower than that on the trailing edge on the upper surface of the airfoil. When $\alpha = 6$ deg., WA model has a similar curve as SST *k*-ω model does. Their results have acceptable agreement with experimental result when x/c is larger than 0.3. On contrary, SA model and the DNS yield a relatively good result when x/c is smaller than 0.3. When $\alpha =$ 12 deg., the freestream become unstable and WA model shows a surprisingly excellent agreement compared to other results.

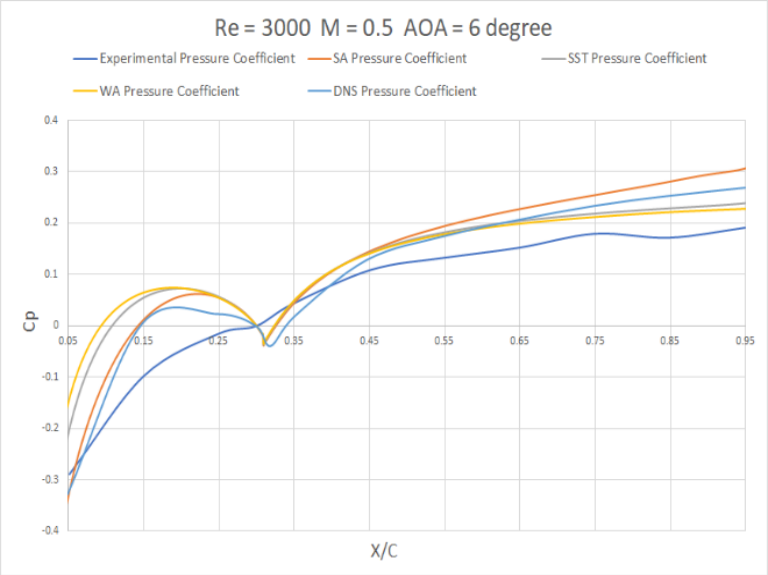

Figure 3. 9 Pressure coefficient on the top surface of the Triangular Airfoil for Re = 3000 and M = 0.5 at AOA = 6 deg.

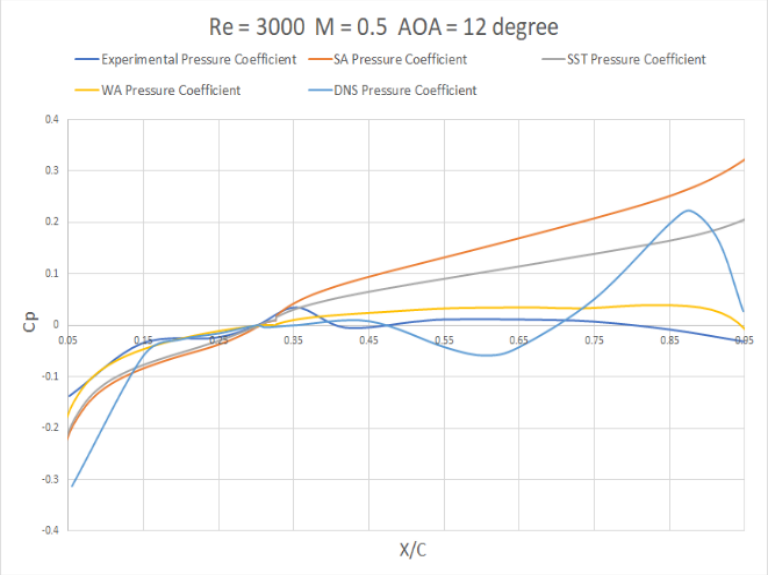

Figure 3. 10 Pressure coefficient on the top surface of the Triangular Airfoil for Re = 3000 and M = 0.5 at AOA = 12 deg.

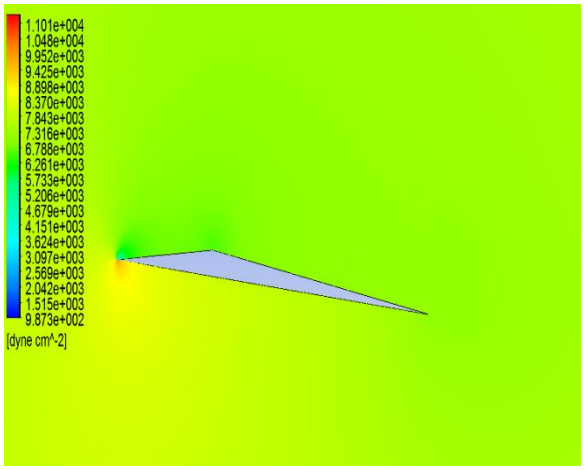

(a) $\alpha = 6°$

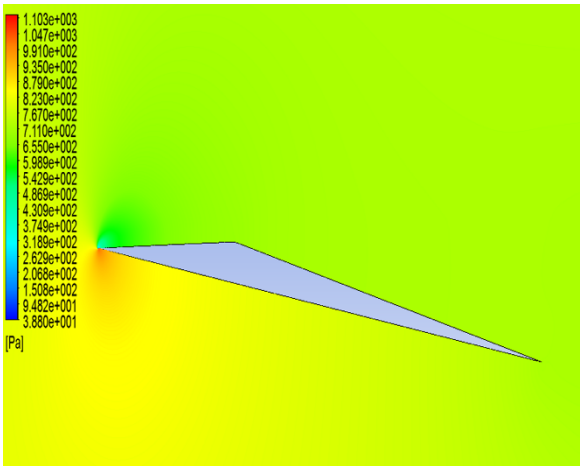

(b) $\alpha = 8°$

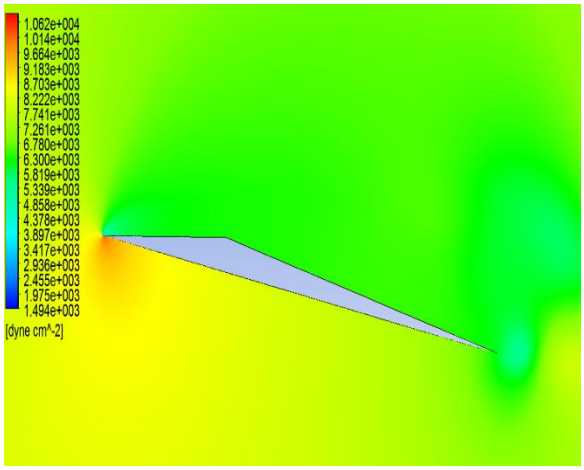

(c) $\alpha = 10°$

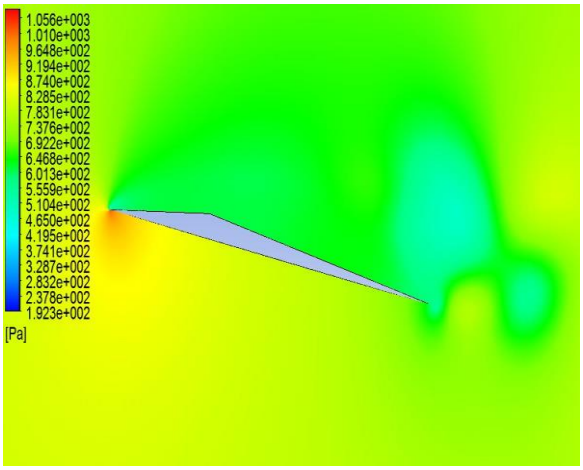

(d) $\alpha = 11°$

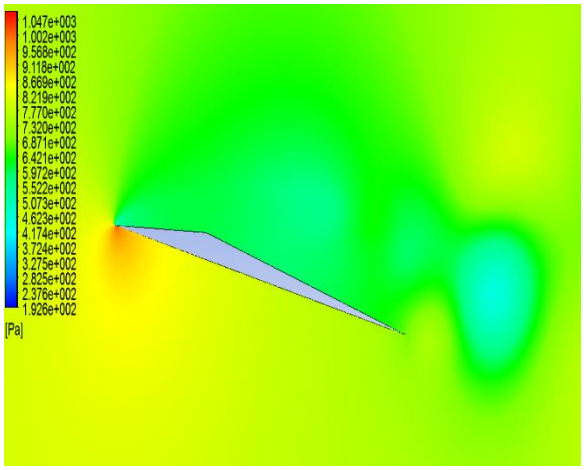

(e) $\alpha = 12°$

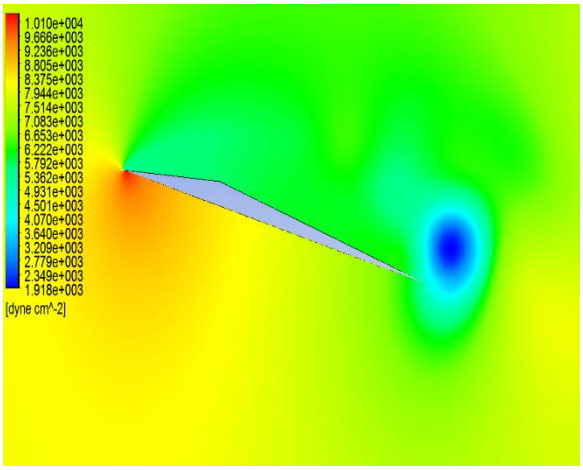

(f) $\alpha = 14°$

Figure 3. 11 Pressure contours around Triangular Airfoil at *Re* = 3000 and *M* = 0.5 for various angle of attack

3.4 Flow Separation

Accurate computation of flow separation is considered very important in drag prediction. From the velocity streamlines, it can be observed that the leading-edge flow separation occurs at $\alpha = 8$ deg. Flow separation occurs at the apex point of the airfoil on the top surface of all AOAs and move toward the leading edge for $\alpha \geq 8$ deg. The flow becomes unsteady at higher angle of attack due to vortex shedding. The leading-edge vortex grows larger as AOA increases then merges with the leading-edge vortex. They forms a large separation bubble on the top of the airfoil and finally covers the majority of the airfoil.

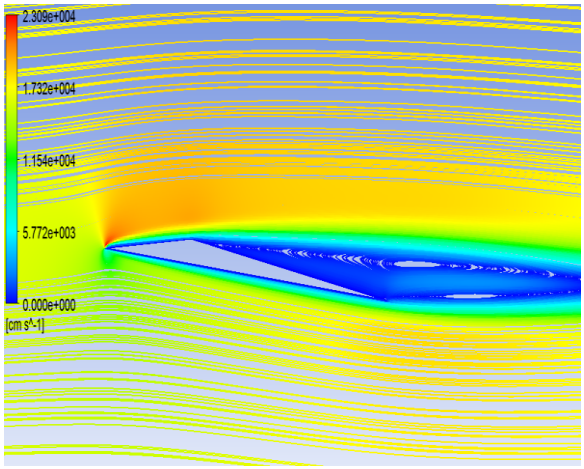

(a) $\alpha = 6°$

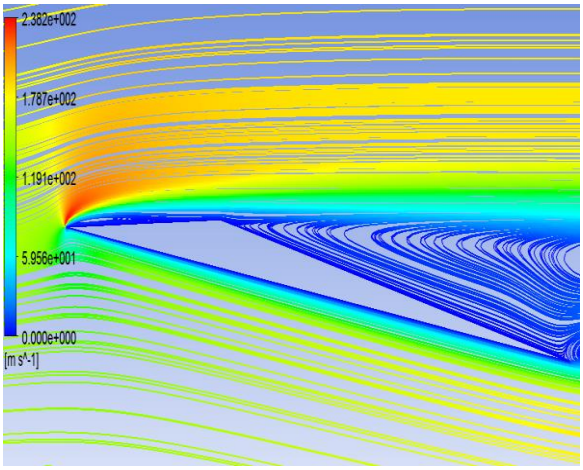

(b) $\alpha = 8°$

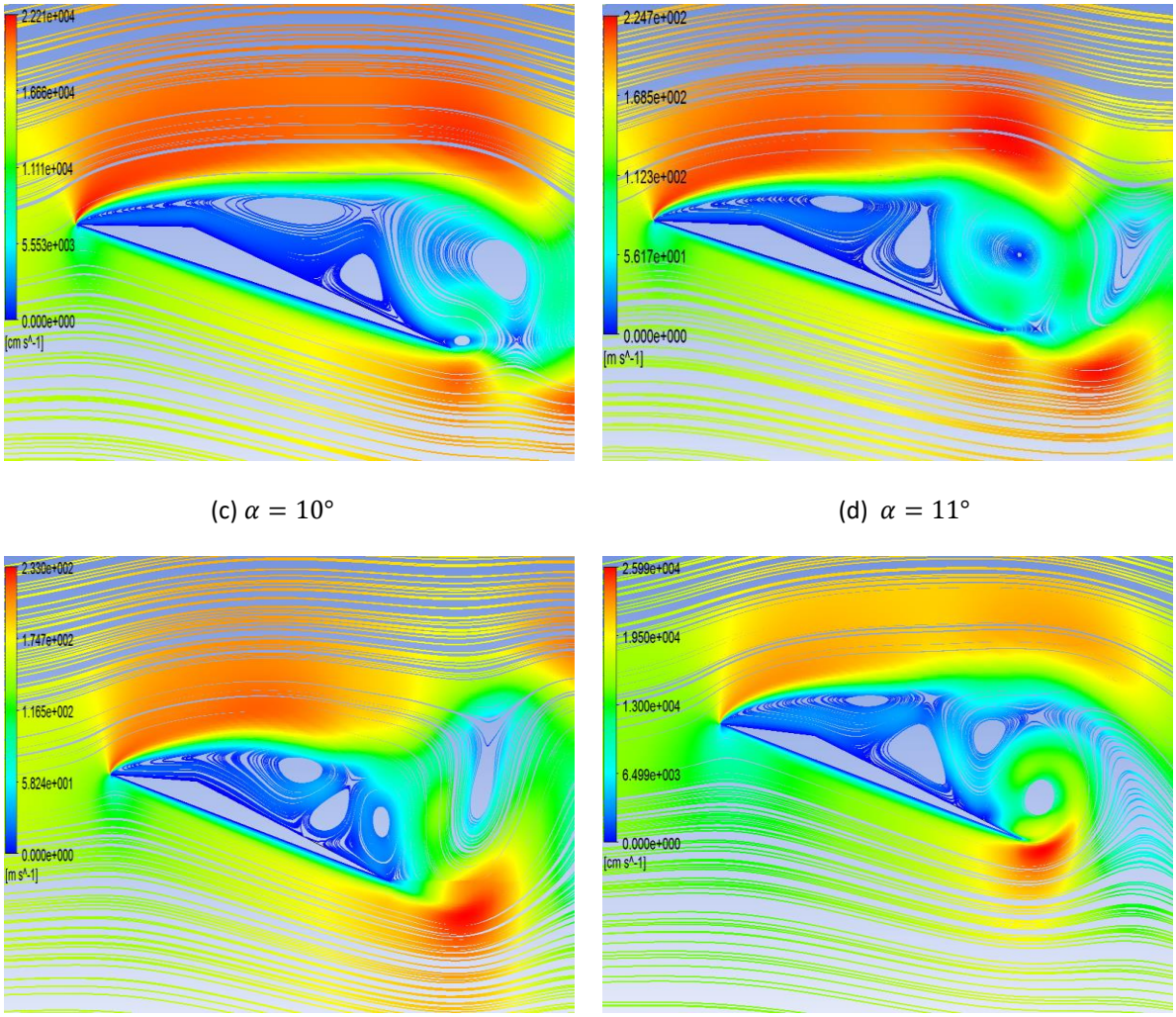

(c) $\alpha = 10°$ (d) $\alpha = 11°$

(e) $\alpha = 12°$ (f) $\alpha = 14°$

Figure 3. 12 Flow separation on the of Triangular Airfoil with increasing angle of attack

3.5 Conclusions

For computed results, for drag and lift coefficient for flow past a triangular airfoil, using WA and SST k-ω models are in good agreement with the experimental data. However, there exists small error between the simulations and experimental results. The experimental results were obtained from Mars Wind Tunnel at Nihon university [3], where the flow was restricted inside a vacuum chamber and the triangular airfoil was going through change in shape due to aeroelastic effects.

All these factors can cause differences between the Mars Wind Tunnel experiment and simulation results. The flow changes from steady to unsteady when $\alpha \geq 8°$. Flow separation is first observed for $6° \leq \alpha \leq 8°$ and the separation point moves from the apex to the leading-edge of the airfoil. As the AOA become larger, the vortex shedding can be observed at the trailing edge become more and more obvious. SA model shows good agreement when $0° \leq \alpha \leq 8°$ while WA shows surprisingly very good agreement for $8° \leq \alpha \leq 14°$. Overall, WA model gives the best agreement with experimental data.

Chapter 4: Analysis of Sweeping Jet Actuator

In this section, the computations for the flow field of a sweeping jet actuator configuration are described and compared with the experimental data.

4.1 Flow Oscillation

Figure 4.1 shows the computed flow oscillations inside the sweeping jet actuator during a time period T. The flow is initialized at $T = 0$ and goes straight from the inlet to the outer flow field which in an ambient fluid. Then it begins to oscillate. Due to the shape of the actuator geometry, an oscillating unsteady flow develops inside the actuator chamber. In addition to the flow exiting from the actuator near the exit plane, there is a backflow which moves in the feedback channels which are on both sides of the chamber. The flow exiting from the actuator oscillates from right to left in a cyclic manner as noted by Vatsa et al. in their computations [5].

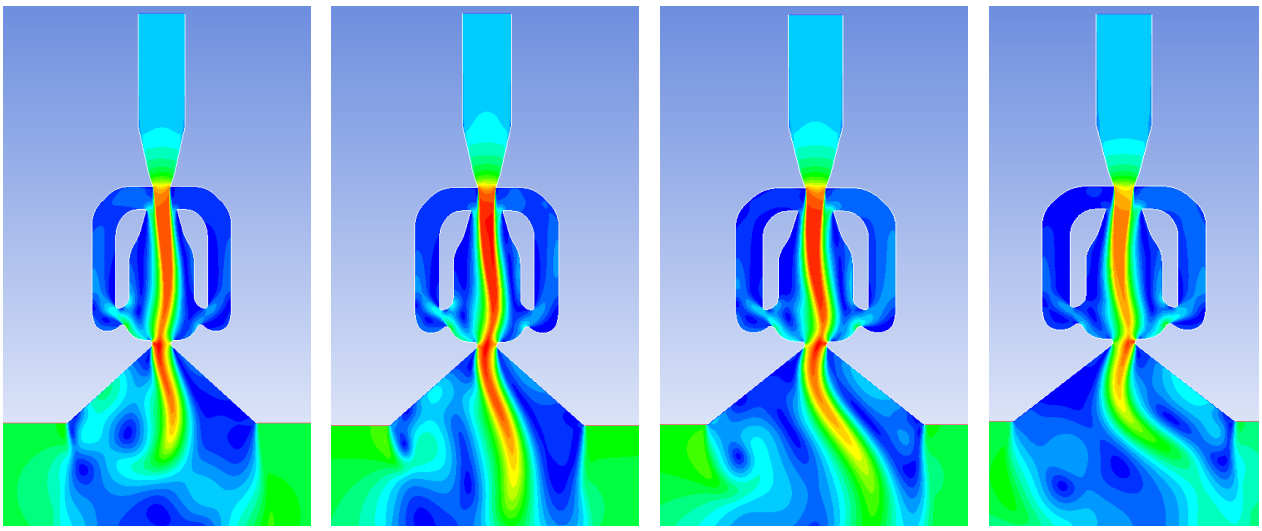

(a) T=1/8 (b) T=2/8 (c) T=3/8 (d) T=4/8

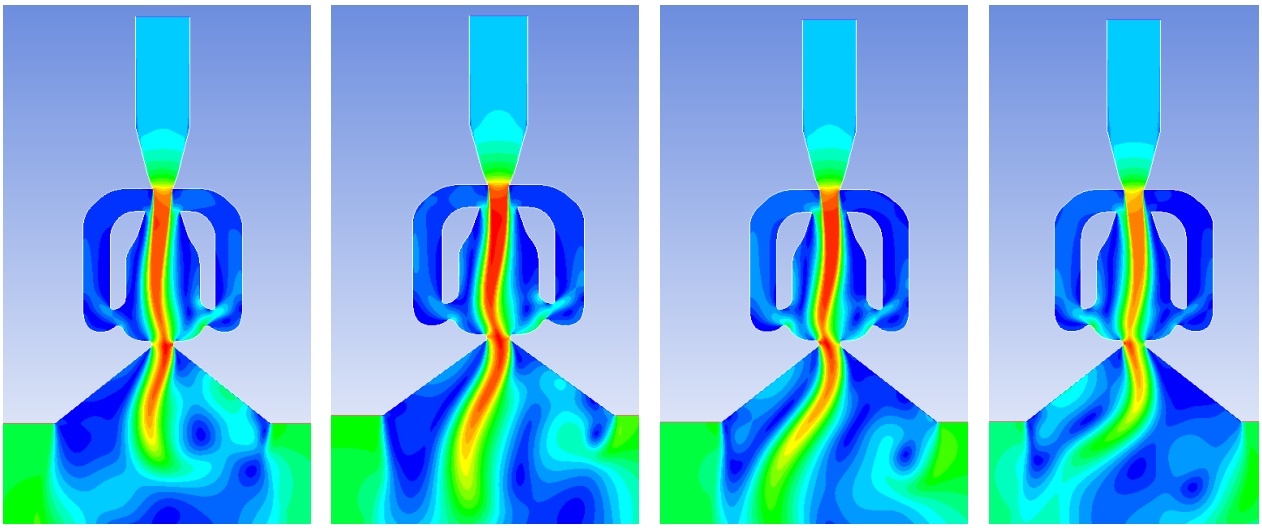

(e) T=5/8 (f) T=6/8 (g) T=7/8 (h) T

Figure 4. 1 Flow oscillations inside the sweeping jet actuator at various time during a time period T

4.2 Velocity Comparison and Velocity Contours

Figure 4.2 shows the geometry and coordinate system. The geometry used in this thesis is the type II curved actuator model which was used by Vatsa et al. [5]. Figure 4.3 shows the comparison of computed results for velocity at Z = 0 mm and Z = 10 mm from FLUENT using k-ε model and experimental data from Vatsa et al. [5]. Figure 4.4 shows the comparison of computed time-averaged velocities and perturbation velocities. The velocities computed from FLUENT with k-ε model are in reasonably good agreement with the experimental data. The maximum difference in velocities between the FLUENT results and experimental results is the minimum value at Z = 0 mm. The computational results for frequency are also in acceptable agreement with the experimental results. The frequency of flow at Z = 0 mm is twice as large as

at Z = 10 mm. Both the maximum velocity at Z = 0 mm and Z = 10 mm is within the acceptable range. Time-averaged velocities and perturbation velocities also show acceptable agreement with the experimental data and reach the similar maximum values at $Z = -10$ mm and Z = 10 mm. As shown in Figure 4.5, the main flow completely attaches the right side of the nozzle and part of the fluid flows back to the left feedback channel. This part of the flows affected flow in the next period. Velocity of the flow is relatively high compared to the nearby flow when it attaches to the nozzle. Therefore, the mesh near the nozzle should be fine to get a more accurate result.

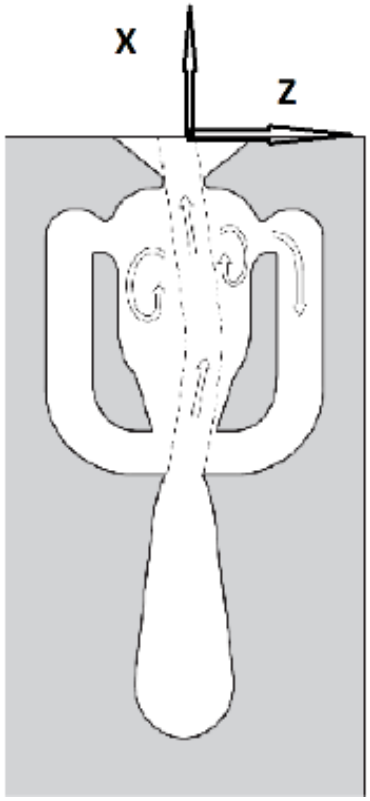

Figure 4. 2 Sweeping Jet Actuator Geometry

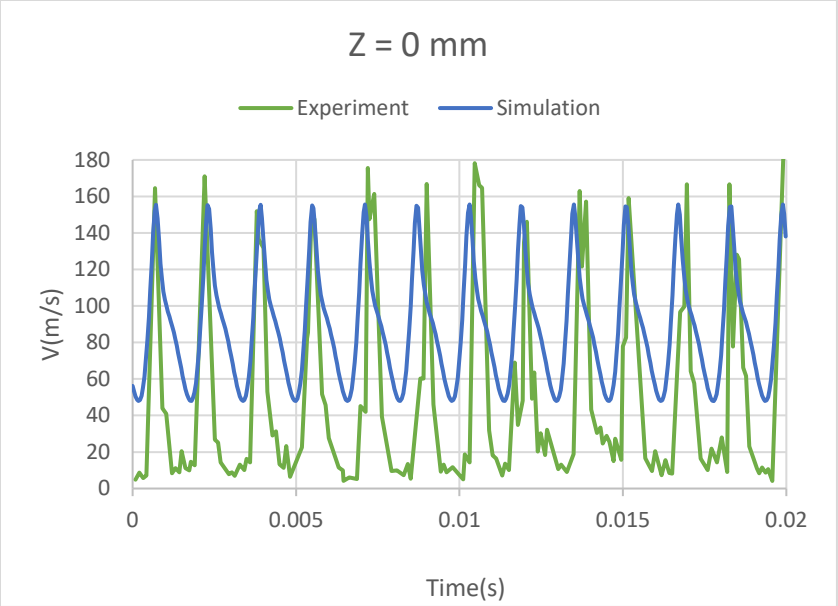

(a) Z = 0 mm

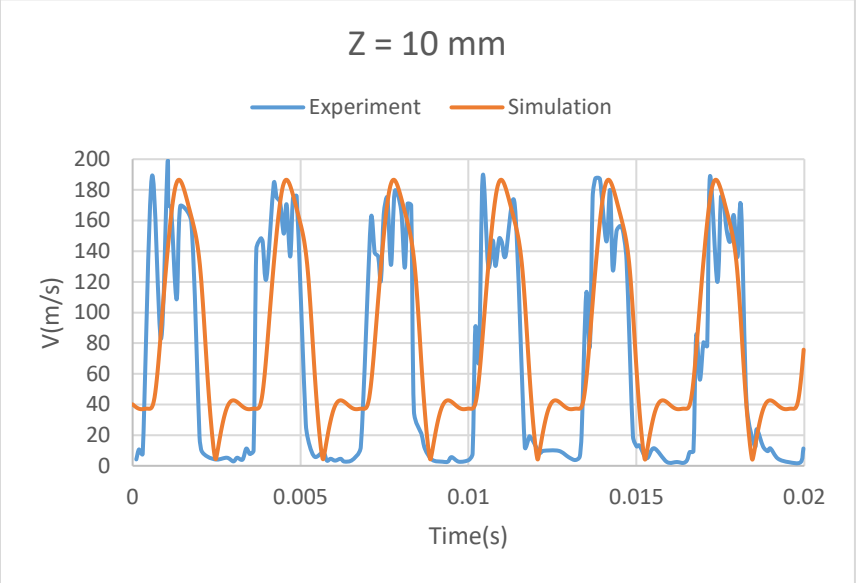

(b) Z = 10 mm

Figure 4. 3 Velocity variation with time at x = 6 mm for *Z* = 0 mm and *Z* = 10 mm for Sweeping Jet Actuator

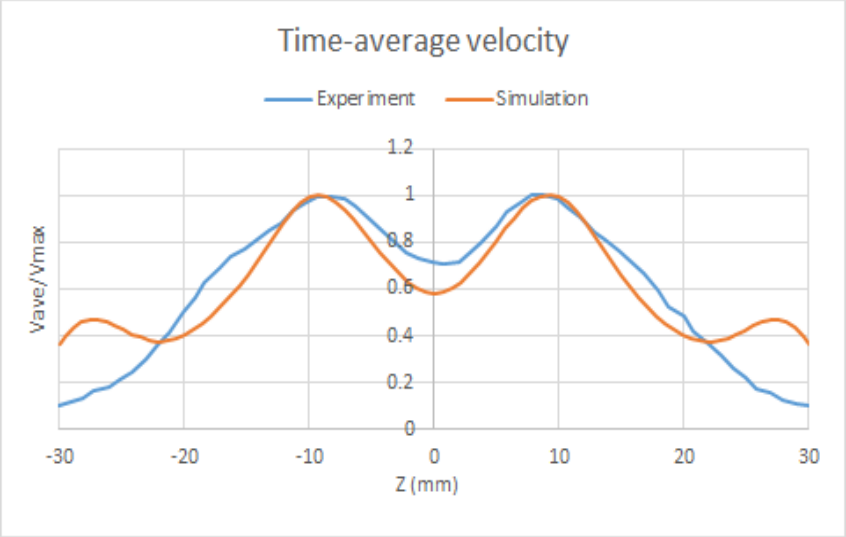

(a)Time-averaged velocities

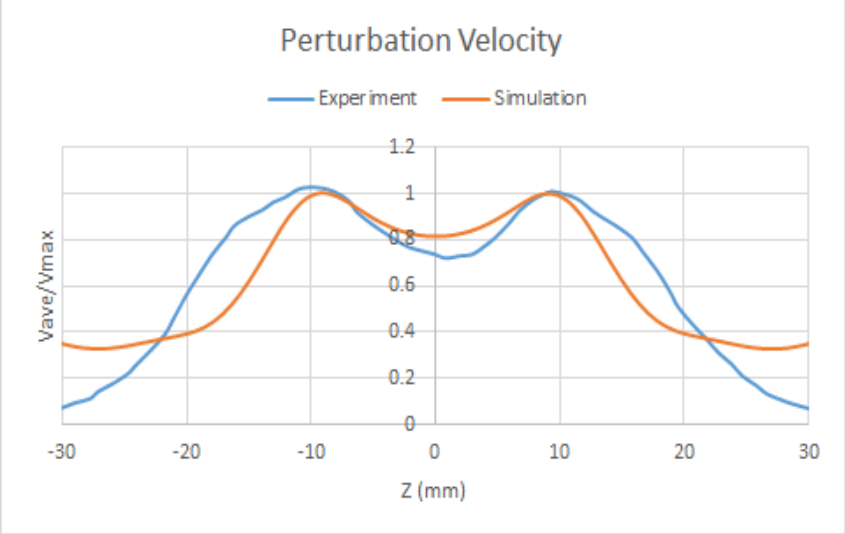

(b) Perturbation Velocities

Figure 4. 4 Time-averaged velocity comparisons for Sweeping Jet Actuator at x = 6 mm

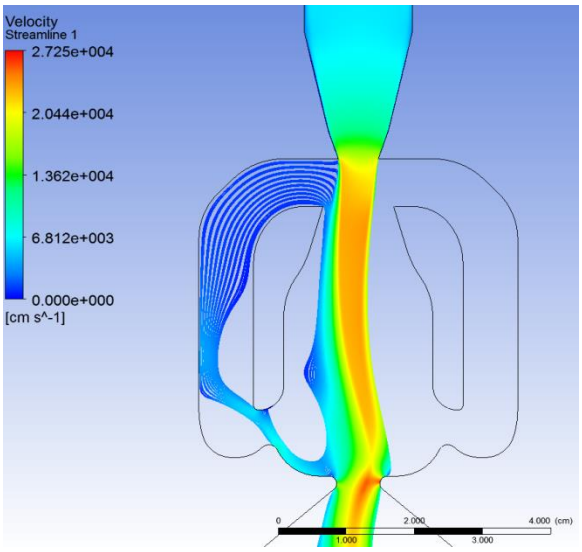

(a) Streamlines of the flow inside the Sweeping Jet Actuator chamber

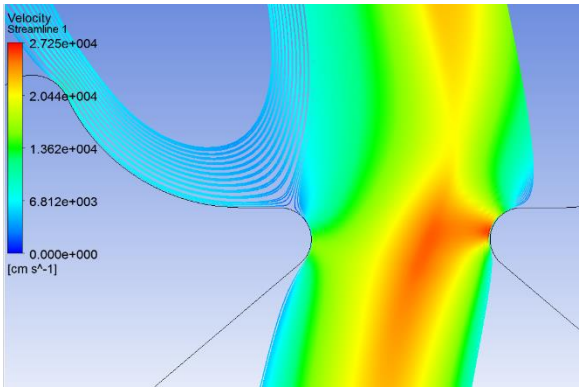

(b) Streamlines of the flow near the Sweeping Jet Actuator nozzle

Figure 4. 5 Streamlines of flow

4.3 Contours of Pressure and Eddy Viscosity

Figure 4.6 shows the contours of pressure for the entire sweeping jet actuator flow field as well as in the nozzle region. The point where the flow attaches inside the nozzle has relatively low

pressure compared to other part of the nozzle. Figure 4.7 shows the contours of Eddy Viscosity in sweeping jet actuator.

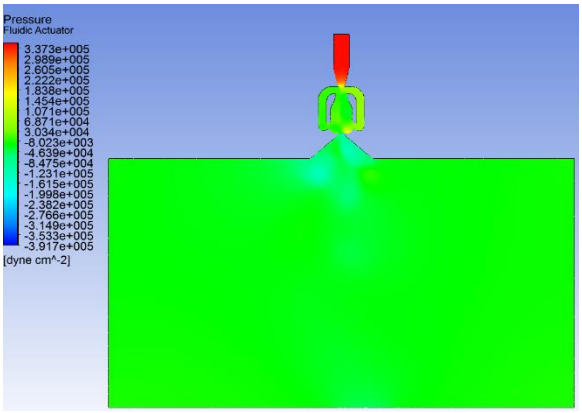

(a) Entire computational domain of Sweeping Jet Actuator

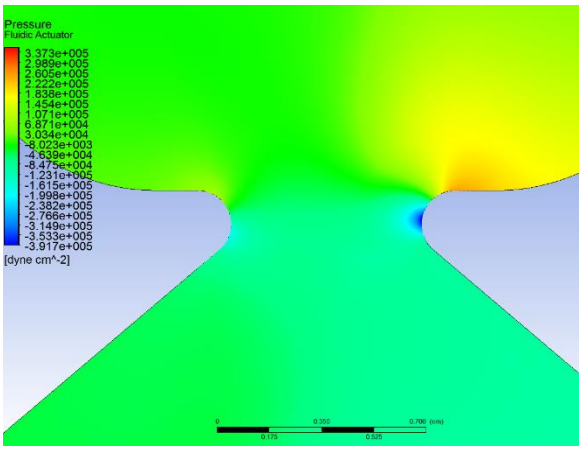

(b) Contour in the nozzle region

Figure 4. 6 Pressure contours inside the Sweeping Jet Actuator

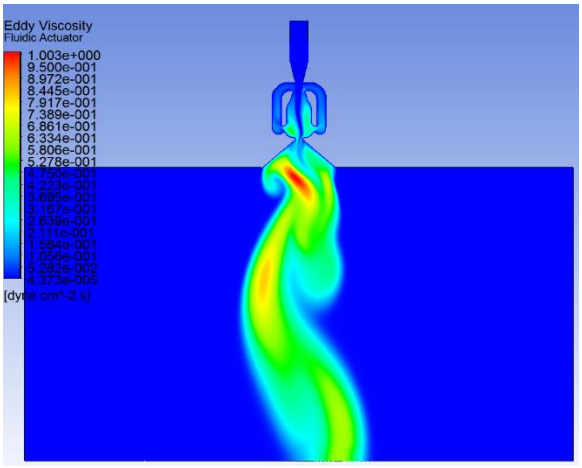

Figure 4. 7 Contour of Eddy Viscosity in the computational domain of Sweeping Jet Actuator

4.4 Conclusions

Numerical simulations were performed using FLUENT to compute the unsteady flow field generated by a sweeping jet actuator and compare it with the experimental data. The simulations provide useful information about the flow physics in the internal and external regions of the sweeping jet actuator. The bi-stable feedback mechanism that produces sweeping oscillatory jet is captured by the visualization software CFD Post. The frequency of flow at Z = 0 mm and Z = 10 mm shows good agreement with experimental data. Overall the agreement of the computed time-averaged mean and perturbation velocities with measurements for the sweeping jet actuator is acceptable.

Chapter 5 Conclusions

The flow fields past a Triangular Airfoil and in a Sweeping Jet Actuator are investigated by numerical simulations using ANSYS FLUENT by solving the RANS equations with SA, *k-ε,* SST *k-ω* and WA model turbulence models. The computations are compared with the experimental data where available. Overall, good agreement is obtained with the experimental and computational results reported in the literature for both configurations.

The flow field of a triangular airfoil is simulated at $Re = 3000$ and $M = 0.5$ for nine different angles of attacks and with three different turbulence models (SA, SST *k-ω* and WA) with the RANS equations to examine the aerodynamic characteristics and flow physics of the airfoil in low Reynolds number compressible flow of the Martian atmosphere. The three turbulence models – SA, SST *k-ω* and WA give acceptable accuracy for both lift and drag coefficient predictions. When $\alpha \geq 8°$, the numerical results show the nonlinear aerodynamic characteristics of the triangular airfoil at high angles of attack, and the flow changes from steady to unsteady. The simulation from $8° \leq \alpha \leq 14°$ diverged using the steady solver. Therefore, all results from $8° \leq \alpha \leq 14°$ were computed using the transient solver. The results from WA model were most accurate when compared to the experimental data followed by those from SST *k-ω* and SA model. Additionally, WA model is twice more efficient in computations compared to SST *k-ω* model, being a one-equation model. In summary, the computations show that WA model can be effectively used to capture the details of the triangular airfoil flow field accurately and efficiently. It is more accurate than the SA model and is competitive with the SST *k-ω* model. Surprisingly DNS results show enormous difference with the experimental results for $\alpha \geq 6°$; The reason for enormous difference between DNS and experimental result for $\alpha \geq 8°$ is that the side-wall effects changed the flow field and altered the reattachment physics.

The computational results show that the sweeping jet actuator is potentially a good device for flow control applications. Computational results using the RANS equations with k-ε model have acceptable agreement with the experimental data. It should be noted that the computational model is 2D while the experiment is 3D. Future work should focus on simulating the effect of a series of sweeping jet actuators on external flow over an aerodynamic configuration of practical interest to examine the effectiveness of such AFC devices for separation control. Parametric studies should be conducted to determine the optimum spacing between actuator arrays to achieve the desired control authority.

Overall, good agreement is obtained with the results reported in the literature for both the configurations.

References

1. H. P. Horton, “Laminar Separation Bubbles in Two- and Three-Dimensional Incompressible Flow,” Ph.D. Thesis, University of London, 1968.

2. Woszidlo, R., and Wygnanski, I., “Parameters Governing Separation Control with Sweeping Jet Actuators,” AIAA Paper 2011-3172, June 2011.

3. Okamoto, M., “An Experimental Study in Aerodynamic Characteristics of Steady and Unsteady Airfoils at Low Reynolds Number,” Ph.D. Thesis, Nihon Univ., Tokyo, 2005.

4. Munday, P. M., Taira, K., Suwa, T., Numata,D., and Asai, K. "Nonlinear Lift on a Triangular Airfoil in Low-Reynolds-Number Compressible Flow," Journal of Aircraft, Vol. 52, No. 3, 2015, pp.924-931.

5. Vatsa, V., Koklu, M., and Wygnanski, I., “Numerical Simulation of Fluidic Actuators for Flow Control Applications. 6th AIAA Flow Control Conference, June 2012, doi:10.2514/6.2012-3239.

6. Spalart, P. R., and Allmaras, S. R., “A One-Equation Turbulence Model for Aerodynamic Flows,” AIAA Paper 92-0439, Jan. 1992.

7. Menter, F. R., “Two-Equation Eddy-Viscosity Turbulence Models for Engineering Applications,” AIAA Journal, Vol. 32, No.8, 1994, pp.1598–1605, Bibcode: 1994 AIAA J.32.1598M, doi:10.2514/3.12149.

8. Chien, K.-Y., “Predictions of Channel and Boundary-Layer Flows with a Low-Reynolds-Number Turbulence Model", AIAA Journal, Vol. 20, No. 1 ,1982, pp. 33-38.

9. Han, X., Wray, T. J., and Agarwal, R. K., "Application of a New DES Model Based on Wray-Agarwal Turbulence Model for Simulation of Wall-Bounded Flows with Separation," AIAA Paper 2017-3966, AIAA Aviation Forum, Denver, 5-9 June 2017.

10. Datta, A., Roget, B., Griffiths, D., Pugliese, G., Sitaraman, J., Bao, J., Liu, L., and Gamard, O., “Design of a Martian Autonomous Rotary-Wing Vehicle,” Journal of Aircraft, Vol. 40, No. 3, 2003, pp. 461–472, doi:10.2514/2.3141.

11. Zhang, H., Fang, J, Revell, A., Zhong, S., Moulinec, C., Emerson, D., and Bai, P., “Aerodynamic Characteristics of Airfoil at Low Reynolds Number in Martian Atmosphere,” Proc. of PARCFD 2018 Conference, Indianapolis, May 2018.

Vita

Han Yang

Degrees M.S. Mechanical Engineering, Dec 2018
B.S. Vehicle Engineering, June 2016

Birth of Place Shishi, Fujian, China

Dec 2018